ORIGINAL ARTICLE

A comprehensive sintering mechanism for TBCs-Part I: An overall evolution with two-stage kinetics

Guangrong Li | Hua Xie | Guanjun Yang | Gang Liu | Chengxin Li | Changjiu Li

State Key Laboratory for Mechanical Behavior of Materials, School of Materials Science and Engineering, Xi'an Jiaotong University, Xi'an, Shaanxi Province, China

Correspondence:
Guanjun Yang, State Key Laboratory for Mechanical Behavior of Materials, School of Materials Science and Engineering, Xi'an Jiaotong University, Xi'an, Shaanxi, China.
Email: ygj@mail.xjtu.edu.cn

Abstract

A comprehensive sintering mechanism for lamellar thermal barrier coatings was reported experimentally and theoretically in this study. To begin with, an overall property evolution with two-stage kinetics was presented during thermal exposure. The increase in mechanical property at initial thermal exposure duration (stage-I) was much faster with respect to that in the following longer duration (stage-II). At the stage-I, the in situ pore healing behavior revealed that the significant faster sintering kinetics was attributed to the rapid healing induced by multipoint connection at the intersplat pore tips, as well as a small quantity of the narrow intrasplat cracks. At the following stage-II, the residual wide intersplat pore parts and the wide intrasplat cracks decreased the possibility of multiconnection at their counter-surfaces, resulting in a much lower sintering kinetic. Moreover, a structural model based on the microstructure of plasma sprayed YSZ coatings was developed to correlate the microstructural evolution with mechanical property. Consequently, the model predicted a two-stage evolutionary trend of mechanical property, which is well consistent with experiments. In brief, by revealing the pore healing behavior, this comprehensive sintering mechanism shed light to the structure tailoring toward the advanced TBCs with both higher thermal-insulating effect and longer life time.

KEYWORDS
ceramic coatings, lamellar structure, mechanical and thermal properties, two-stage kinetics, ultrahigh temperature sintering

1 | INTRODUCTION

Thermal barrier coatings (TBCs)[1,2] find extended application in both aircraft engines and land-based gas turbines to protect the metal components in hot-section. The TBCs commonly exhibit a multilayered-structure.[1,3,4] Firstly, a intervening bond-coat is deposited on superalloy to facilitate strong adhesion between substrate and a top-coat. Subsequently, the ceramic top-coat is deposited to provide the thermal insulating function.[3,5] A common material for the top-coat is the yttria-stabilized zirconia (YSZ), since it exhibits a low thermal conductivity [~2.5 W·(m·K)$^{-1}$][6] and a high thermal expansion coefficient (~11 × 10^{-6} K^{-1}).[7]

Plasma spraying (PS) continues to dominate the preparation of the top-coat owing to its features of fast, flexible, and cost-effective deposition as well.[8,9]

In addition to the intrinsic low thermal conductivity of the YSZ material, the thermal barrier performance of a PS-YSZ coating depends significantly on its unique porous structure, which is formed because of the spraying process. During plasma spraying, a stream of molten or partially molten particles impact on substrate followed by lateral flattening, rapid solidification, and cooling.[10] Consequently, a plasma sprayed coating exhibits typical lamellar microstructure with intersplat pores, intrasplat cracks, as well as globular voids.[7,11] The intersplat pores generally

refer to the imperfect bonding between splats, whereas the intrasplat cracks are generated during splat quenching.[7,11,12] Moreover, the intersplat pores and the intrasplat cracks are also termed as two-dimensional (2D) pores, which lead to the nonlinear elastic behavior as a result of their open and close under load.[13] Additionally, the microstructure (eg, sizes and separations of these 2D pores) of the PS-YSZ coatings is highly dependent with the morphologies of starting powders[14-16] and the process conditions.[5,13] In brief, a PS-YSZ coating exhibits a continuous pore network in a continuous material, since most of the intersplat pores are connected with the intrasplat cracks.[17,18] Consequently, with respect to the bulk YSZ material, this unique microstructure confers >1/2 decrease of the through-thickness thermal conductivity [~1 W·(m·K)$^{-1}$][3,11,14,19,20] and approximately >1/2 drop of the in-plane Young's modulus.[9,19,21,22]

The high operating temperature of engines often has a detrimental effect on the PS-YSZ coatings, in particular, in sintering-induced stiffening[9,11,23] as well as a decrease in the thermal insulation capacity.[11,23] The associated microstructural change is mainly the combination of intersplat locking and splat stiffening because of the healing of intrasplat cracks.[11,20,24] The scale of globular voids remains unchanged during sintering process owing to the fact that they are mainly large closed pores with a near-spherical morphology.[25,26] In brief, this microstructural evolution related to the 2D pores is responsible dominantly for the adverse effect on the performance degradation of the sintered PS-YSZ coatings.[16]

The common feature of the aforementioned papers is that a rapid increase in properties at initial thermal exposure duration slows down distinctly at the following extended duration. Therefore, the sintering kinetics of PS-YSZ coatings is sensitive to the thermal exposure stages. However, the reasons and the associated microstructural evolution coherent to the stage-sensitive kinetics are still not well understood. Therefore, it is essential to comprehensively understand the sintering mechanism, including the initial ultrafast sintering kinetics, so as to give enough supports for the structural tailoring of the PS-YSZ coatings.

The sintering behavior of the PS-YSZ coatings is material and structure specific. Toward this orientation, Cipitria et al.[7,27] developed a systematic sintering model with connected inter/intra splat pore network. The obtained sintering process seems quantitatively understood only during a relatively long duration. Unfortunately, the model prediction cannot be well consistent with the stage-sensitive sintering kinetics obtained by experiments. Actually, regarding the PS-YSZ coatings, few literatures focused on the sintering mechanism with varying kinetics. Therefore, the comprehensive understanding on the sintering behavior of the PS-YSZ coatings, in particular, on the ultrafast kinetics during initial thermal exposure, is still a challenge up to now.

The purpose of this work was to reveal a comprehensive sintering mechanism concerning the stage-sensitive kinetics. To begin with, the mechanical property during thermal exposure has been determined. Subsequently, a two-stage evolutionary trend, as well as the associated microstructural changes was examined. In addition, a structural model based on the PS-YSZ coatings was developed to correlate the microstructural evolution with the mechanical property. In a companion paper, a detailed examination on the pore surface was carried out to account for the ultrafast sintering kinetics when initially exposed. Based on these results, a comprehensive sintering mechanism for lamellar TBCs could be revealed.

2 | EXPERIMENTAL PROCEDURE

2.1 | Materials and sample preparation

A commercially available hollow spheroidized 8 wt% YSZ powder (HOSP, −75 to +45 μm, Metco 204B-NS, Sulzer Metco Inc., Westbury, NY) was used to deposited YSZ coatings and individual splats. The plasma spraying equipment is a commercial system (GP-80, 80 kW class, Jiujiang, China). The spray parameters were shown in Table 1. After deposition, free-standing YSZ coatings, with a dimension of Φ20 mm × 0.5 mm, were obtained through post-spray dissolution of the stainless steel substrate by a hydrochloric acid solution.

2.2 | Thermal exposure of samples

In real service condition, it may be extremely difficult to evaluate the sintering effect on the microstructural evolution, since the service environment can be very harsh.

TABLE 1 Plasma spray parameters for individual splats and coatings

Parameters	Individual splats	Coatings
Plasma arc voltage/V	70	70
Plasma arc current/A	600	600
Flow rate of primary gas (Ar)/L min^{-1}	50	50
Flow rate of secondary gas (H$_2$)/L min^{-1}	7	7
Flow rate of powder feeding gas (N$_2$)/L min^{-1}	6	6
Spray distance/mm	110	110
Torch traverse speed/mm s^{-1}	1000	800
Substrate preheating temperature (°C)	250	/

Instead, isothermal heat treatment[3,14] and thermal cycling test[28] become attractive to investigate the sintering effect. In particular, the isothermal heat treatment has several advantages owing to its high-temperature accuracy, ease of temperature control, as well as cost-effective operation. On the other hand, regarding the long life time (eg, 8000-16 000 h) of TBCs at their working temperatures (eg, ~1000°C),[29] it is necessary to adopt a higher temperature to accelerate the sintering process. Therefore, in this study, the free-standing coatings were isothermally heat treated in a furnace to 1000°C and 1300°C. After progressively holding for different durations, the samples were cooled down to room temperature. In order to avoid the unexpected coating structural degradation induced by fast temperature changes, the heating rate and the cooling rate were fixed at a relatively low rate of 10°C/min. Based on previous reports,[30,31] the heating duration by using this heating rate (10°C/min) is too short to trigger the phase transformation.

2.3 | Microstructural characterization of YSZ samples

Cross-sectional samples of the coatings and individual splats were prepared using a focused ion beam system (FIB, Helios NanoLab600, FEI, Hillsboro, OR), in order to prevent damage to the initially present bonds. Quasi in situ morphological observations on the 2D pores were made using a scanning electron microscopy (SEM) system (TESCAN MIRA 3, Brno, Czech Republic). The intersplat pores and the intrasplat cracks were examined on the fractured cross-section and the surface of YSZ coating samples (Φ20 mm × 0.5 mm), respectively. The detailed procedure is described as follows. To begin with, a target position was found at a high magnification. Subsequently, the magnification decreased gradually until the whole sample could be observed. Meanwhile, the target position was fixed at this magnification by measuring its coordinates. After thermal exposure, the corresponding coordinates were used to find the target position. With this approach, a quasi in situ observation can be achieved.

Residual 2D pore length density, defined as the total length of 2D pores in unit area, was determined in this work. The length densities of intersplat pores and intrasplat cracks were obtained from the polished cross-section and the polished surface of YSZ coatings, respectively. Furthermore, width distribution of the intrasplat cracks was obtained statistically from the free coating surface. At least 50 SEM images at a magnification of ×5000 were determined. The details to determine the 2D pore length density and the crack width distribution can be found elsewhere.[32] Intersplat bonding ratio and mean splat thickness of the as-deposited coating were determined through structural visualization described elsewhere.[33] This involves having an Al(NO$_3$)$_3$ saturated solution infiltrate into the YSZ coatings. Subsequently, the infiltrated samples were dried and heated to 550°C, held at this temperature for 30 minute, and then cooled down to room temperature. After repeating this procedure for more than 10 times, enough alumina will be left in the pores between splats. Then, using energy-disperse X-ray spectroscopy, the mean bonding ratio and the mean splat thickness could be determined. In addition to the structural visualization, the splat thickness can also be determined from the cross-section of individual splats.

2.4 | Measurement of mechanical property

The macroscopic Young's moduli in the in-plane direction was determined using a three-point bending (3PB) test system (Instron 5943, Boston, MA).[34] During this test, the Young's moduli E can be obtained from the following formulas:

$$w = \frac{PL^3}{48D} \quad (1)$$

$$D = \frac{Eh^3}{12(1 - v^2)} \quad (2)$$

where P is the load applied to the middle of the span, L is the span between two supports, D is the bending stiffness, E is the Young's moduli of the coating, h is the coating thickness, and v is the Poisson's ratio of the coating.

The microscopic Young's moduli of the YSZ coatings was determined using a Knoop indentation test system (Buehler Micromet 5104; Buehler Corporation, Lake Bluff, IL). The test was performed at a load of 300 g and holding time of 30 s. Knoop indentation is based on the measurement of the elastic recovery of the in-surface dimensions of Knoop indentations.[35] During unloading, the elastic recovery reduces the length of the minor diagonal of the indentation impression (b'), whereas the length of the major diagonal of the indentation impression (a') remains relatively unaffected. The ratio of the major (a) to minor (b) diagonals of the Knoop indenter is 7.11. The formula for determining the Young's modulus is:

$$E = \frac{\alpha H}{\left(\frac{b}{a} - \frac{b'}{a'}\right)} \quad (3)$$

where α is a constant (0.45), H is hardness, a' and b' are the lengths of the major and minor diagonals of the indentation impression, respectively, and b/a is 1/7.11.

The in-plane Young's moduli was determined from the polished surface of the coating samples. In contrast, the out-plane Young's moduli was obtained from the polished cross-section, making sure that the minor diagonal was parallel to the deposition direction.

3 | EXPERIMENTAL RESULTS AND DISCUSSION

3.1 | Overall evolution of the young's modulus

The evolution of both the macroscopic and microscopic Young's modulus of YSZ coatings is shown in Figure 1. It can be observed that the macroscopic Young's modulus is distinctly lower than the microscopic Young's modulus. This is consistent with previous reports.[9,11,18,36] The reason is that the macroscopic Young's moduli is a global reflection of the strain tolerance of a whole coating structure. Consequently, many large-scale pores may also have a significant effect on the macroscopic Young's moduli. This is consistent with previous report,[13] which revealed a significant effect of the pore size on the elastic property. Regardless of this difference, both the macroscopic and the microscopic Young's modulus exhibited an ultrafast increase rate at initial short duration. Subsequently, the increase rate slowed down significantly during the following longer duration. Consequently, the initial short duration finished most increment of the Young's modulus. This phenomenon is consistent with those sintering investigations mentioned in the Introduction.[9,11,23]

3.2 | Two-stage evolutionary trends during sintering procedure

Figure 2 shows the evolutionary trend of the Young's modulus as a Ln-t curve. In order to show the overall trend, 0.1 hour was used to represent the as-deposited state which

actually corresponded to 0 hour. It can be observed that the total evolution was divided into two stages approximately, termed as stage-I and stage-II. Moreover, the divided boundary was located around 10 hours, which is consistent to the shrinkage results.[37] It is obvious that the increase rate of the Young's modulus at the stage-I was much larger than that at the stage-II. Another noteworthy phenomenon with respect to the two-stage evolutionary trend was that a higher temperature resulted in a shorter stage-I.

Figure 2A-2, B-2,A-3, B-3 exhibit a total increment and an increment per hour of the Young's modulus in these two stages, respectively. Corresponding to the much larger increase rate in the stage-I (see Figure 2A-1, B-1), a majority increment of the Young's modulus finished during this stage. In the case of the mean increment per hour, the value at the stage-I exhibited hundreds of times with respect to that at the stage-II. In addition, the increase rate in the out-plane direction was larger than that in the in-plane direction. Consequently, the resulted microscopic Young's modulus in the out-plane direction exceeded those in the in-plane direction after the stage-I. It is known that the mechanical property of the PS-YSZ coatings depends dominantly on the 2D pore network.[18] The pore healing behavior is thereby necessary to be revealed, in order to further understand the two-stage evolutionary trend.

3.3 | Morphological characteristics of the 2D pores

Figure 3 shows morphologies of the 2D pores at the as-deposited state. It can be observed that most of the
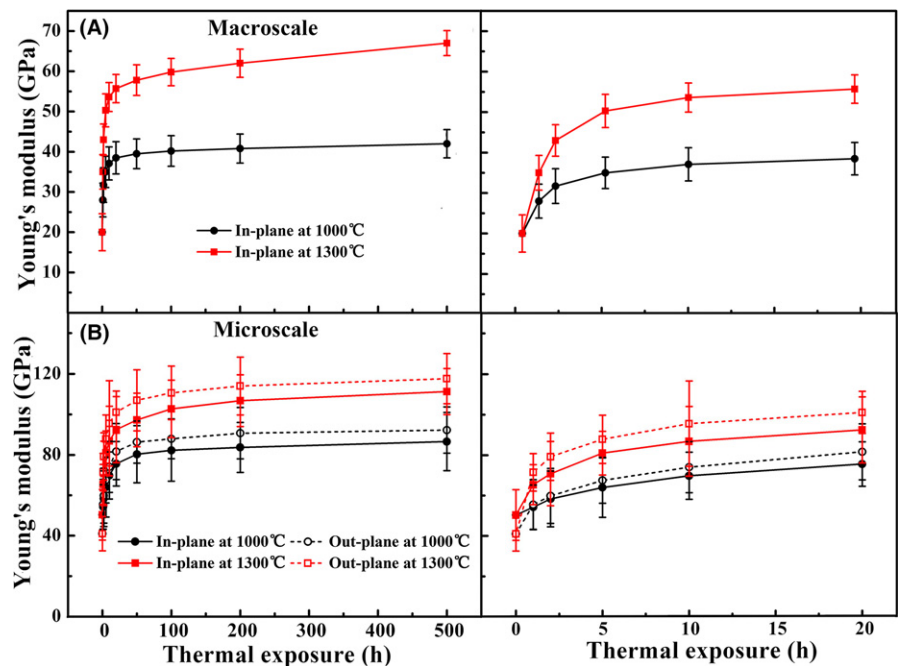

FIGURE 1 Evolution of the macroscopic and microscopic Young's modulus after thermal exposure: (A) macroscopic Young's modulus and (B) microscopic Young's modulus [Color figure can be viewed at wileyonlinelibrary.com]
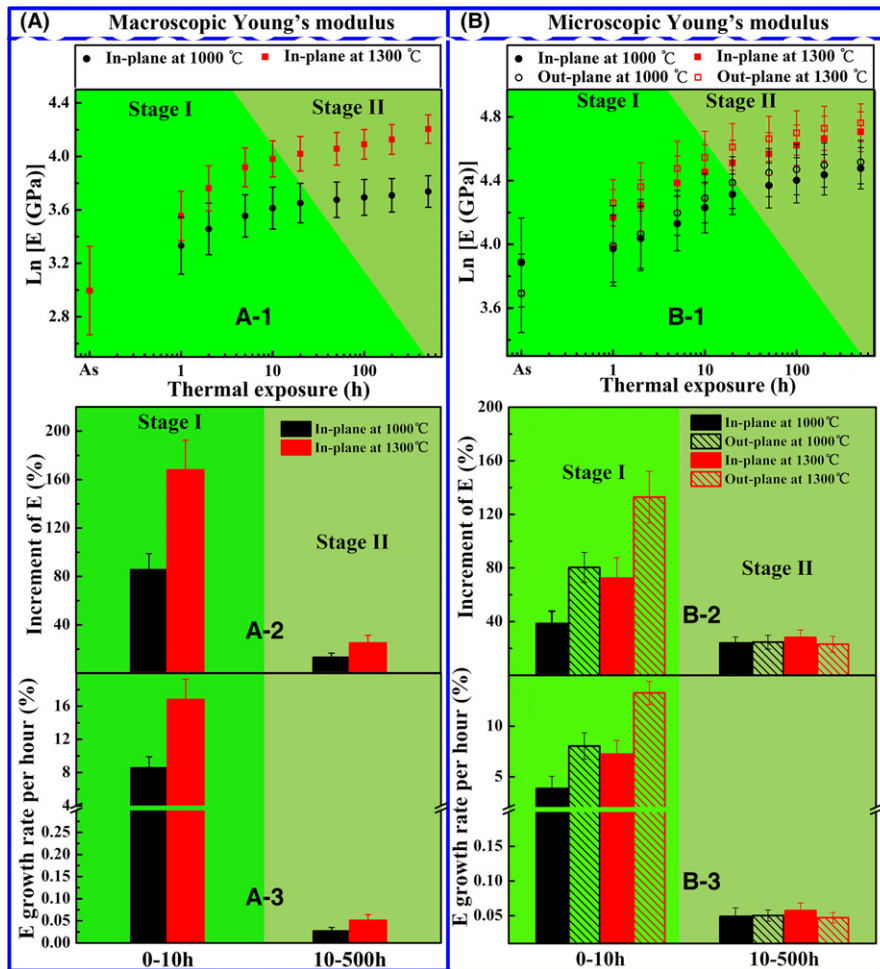
FIGURE 2 A two-stage evolutionary trend of the Young's modulus. (A) and (B) correspond to the macroscopic and the microscopic Young's modulus, respectively. (A-1, B-1) show the evolution of Young's modulus as Ln-t after thermal exposure. In order to show the overall trend, 0.1 h was used to stand for the as-deposited state (short for As) without heat treatment. (A-2, B-2) and (A-3, B-3) refer to the total increment and increment per hour of the Young's modulus in two stages, respectively. The dark and light regions correspond to the stage-I and the stage-II, respectively [Color figure can be viewed at wileyonlinelibrary.com]

intrasplat cracks run through the splat with an almost equally thick morphology (see Figure 3A). In addition, the width of intrasplat cracks can be ranging from tens of nanometers to hundreds of nanometers. However, much different from the intrasplat cracks, the intersplat pores appeared to be primarily wedge-like (see Figure 3B). Additionally, the cross-section of an individual splat bonded to substrate further confirmed the wedge-like morphology of the intersplat pores. This is completely different from the equally thick pore structure as assumed in the reported literatures.[7,27,38] The morphology difference between the intersplat pores and intrasplat cracks may affect the sintering process.

3.4 | Characterization of pore healing procedure

Figure 4 shows evolution of the 2D pore length density of YSZ coatings during thermal exposure. During the overall duration (0-500 hour), the densities of both the intersplat pores and the intrasplat cracks decreased dramatically, suggesting that the healing of 2D pores has a significant effect on the mechanical property.[18] In the case of the Ln-t curve

(see Figure 4B), it is possible to observe that the density of intersplat pores decreased rapidly at the stage-I (0-10 hour), and then the decrease rate slowed down in the stage-II. In contrast, the decrease of the intrasplat cracks was not so distinct as that of the intersplat pores at the stage-I. Based on the statistical results above, it is possible to conclude that the ultrafast sintering kinetics at the stage I was attributed primarily to the significant healing of the intersplat pores.

The quasi in situ healing behavior of the 2D pores in YSZ coatings during the stage-I is shown in Figure 5. It can be observed that the quantity of the crack-tips was much smaller than that of the running-through cracks (see Figure 5A). This is consistent with the morphology of intrasplat cracks observed in Figure 3A, and it confirmed that most of the intrasplat cracks separate the segments completely. In brief, it seems that the widths of intrasplat cracks were in the range of 100-500 nm by and large. The ratio of the crack-tips, as well as the very narrow cracks (<100 nm) is less than 10% with respect to the total statistical cracks. Figure 5A shows the healing evolution of intrasplat cracks with different widths. It can be observed that almost no healing occurred for the wide cracks at the
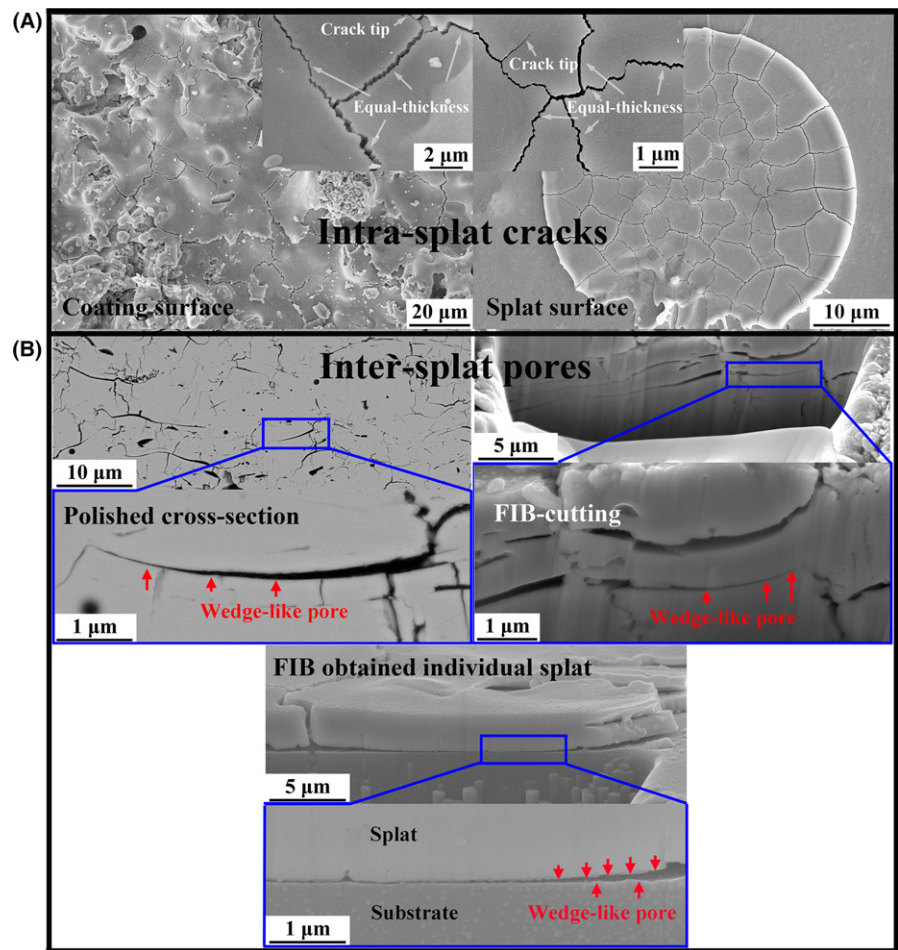
FIGURE 3 The as-deposited morphologies of intrasplat cracks (A) and intersplat pores (B). The intrasplat cracks were examined from the surface of YSZ coatings and an individual splat. The intersplat pores were presented from the cross-sections prepared by both the polishing and the FIB cutting [Color figure can be viewed at wileyonlinelibrary.com]

stage-I (see Figure 5A with width-C). In spite of the significant healing of a narrow crack (see Figure 5A with width-B), an incubation period (>10 hour) is necessary to drive this procedure. In contrast, obvious healing can be observed after a short duration (1 hour) at the crack tip (see Figure 5A width-A). This phenomenon can also be found in Figure 5A with width-C, where a very narrow crack tip was healed after initial duration (<10 hour).

Figure 5B shows the healing evolution of the intersplat pores isothermally exposed at 1000°C and 1300°C. It can be observed that significant healing occurred at the pore tips despite of temperatures. To begin with, a common phenomenon was that the initial smooth splat surface became roughening after thermal exposure. Subsequently, the healing of intersplat pores proceeded by apparent bridge-connection owing to the surface roughening. Consequently, multipoint connection occurred between the counter-surfaces. To sum up, at the stage-I, significant healing occurred at the intersplat pore tips and a small ratio of narrow intrasplat cracks. This is consistent with the statistical results (see Figure 4). The anisotropic healing trends of these 2D pores can account for the anisotropic evolution of the Young's modulus at the stage-I (see Figure 2), since the mechanical property is more sensitive to their

perpendicular 2D pores.[39] The critical role of splat interfaces on the effective properties is consistent with previous reports, which correlated quantitatively the splat interfaces with effective properties at the as-deposited state and the sintered state.[16,20]

Some previous reports suggested that the intrasplat cracks healed preferentially, in particular, at a lower temperature (eg, 1000°C), which seems contradictive to our results. For instance, some examinations, based on small-angle neutron scattering, exhibited a significant healing of intrasplat cracks at a lower temperature (1100°C) after a short thermal duration. At higher temperatures (1300°C and 1400°C), both the healing of intersplat pores and intrasplat cracks occurred.[40,41] Similar results were obtained by Trice et al.[42] based on TEM examination. However, these are consistent with our report based on the following reasons: (i) the width of intrasplat cracks is located in a wide range (see Figure 5A). In contrast, the intersplat pores often exhibit a co-existence of the wide part with the narrow part (pore tips); (ii) At the stage-I, the ultrafast sintering kinetics was attributed to the multipoint connection (multiconnection) of the counter-surfaces, which rapidly decreases the free energy of the whole system. It is known that the sintering is a thermally activated process driven by the
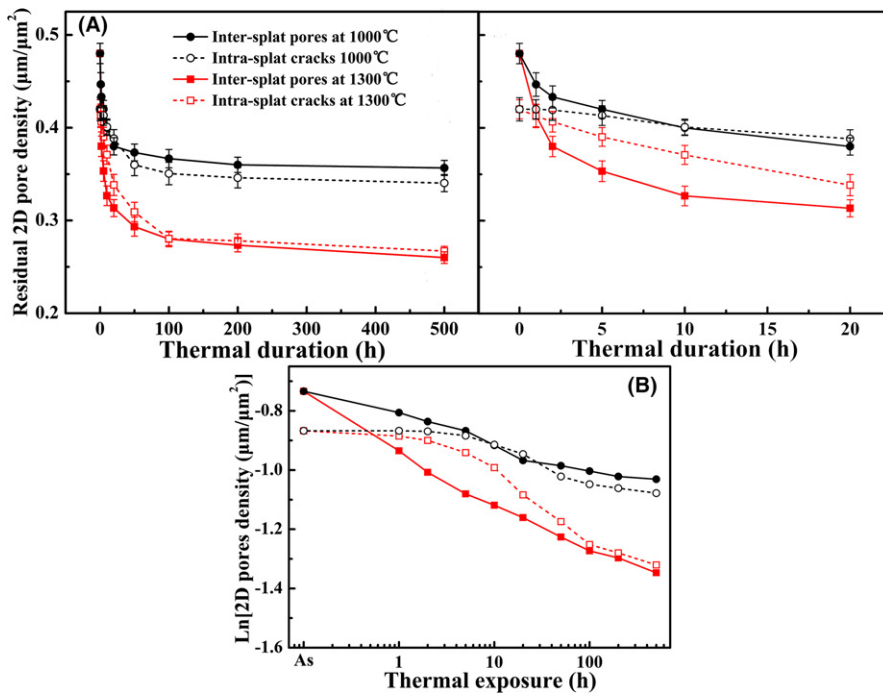
FIGURE 4 Evolution of the 2D pore density during thermal exposure: (A) evolution during different durations and (B) evolution of the 2D pore density shown as the Ln-t [Color figure can be viewed at wileyonlinelibrary.com]

reduction in surface energy.[7,43] The formation of multipoint connection seems to be a good choice, and thus contributes to the extremely high sintering kinetics; (iii) in the case of intrasplat cracks, their counter-surfaces often appear to be coarse in a microview due to the cracking behavior of ceramic materials (see Figure 3A),[44] although these cracks exhibit equal-thickness in an apparent view. That means the multipoint connection is possible to occur on those narrow cracks. In contrast, the counter-surfaces of intersplat pores often have smoother surfaces owing to the already solidified splat.[44] During thermal exposure, the smooth surface becomes roughening (see Figure 5B), which leads to pore tip healing induced by multiconnection. In brief, the multiconnection-induced healing is responsible for the ultrafast sintering kinetics at the stage I. Moreover, this multiconnection-induced healing occurs at almost every intersplat pore tip, as well as a small ratio of very narrow intrasplat cracks; (iv) the roughening of intersplat pore surface is temperature-dependent. A higher temperature leads to a more severe roughening.[45] At a lower temperature (eg, 1000°C), the pore healing at tips occurs at relatively smaller parts owing to the slight roughening. However, for those cracks with very narrow widths (see Figure 5A with Width-C), the initial coarse surfaces facilitate the multiconnection-induced healing. Moreover, different from the healing behavior of intersplat pores which starts from tips, the healing of the narrow cracks may occur all over their parts (see Figure 5A). Consequently, the decrease of the specific surface area of intrasplat cracks may seem comparable with that of the intersplat pores,[40,41] although actually only a small ratio of narrow cracks was healed (see Figure 5A).

At a higher temperature, the roughening of splat surface becomes much more severe. Consequently, the multiconnection-induced healing occurs at a relatively larger part of intersplat pore tips, as well as a small ratio of the narrow intrasplat cracks. This can be account for the phenomenon observed in the above-described reports[40,41,44] that the healing of intrasplat cracks seems preferentially at a lower temperature; (v) the multiconnection-induced healing of the intersplat pores and the intrasplat cracks is responsible for the ultrafast sintering kinetics. However, their mechanisms are different. In the case of intersplat pores, the multiconnection is generated owing to the roughening derived from the faceting of grain surface, grooving of bared grain boundary, as well as columnar grains convex.[45] However, the multiconnection of the intrasplat crack surfaces may be primarily attributed to the initial coarse morphology.[44] Based on the consideration that the quantity of the very narrow cracks is small (<20%), it may be appropriate to conclude that the main structural change at the stage I is the healing of intersplat pores through multiconnection. At the following stage II, the relatively wider counter-surfaces (including the wide intrasplat cracks and the wide residual intersplat pore parts) decrease the possibility of multiconnection. Consequently, the sintering kinetics slows down significantly. It is obvious that the multiconnection-induced fast sintering occurs primarily during the stage I (approximately 10 hour at 1300°C). However, the significant formation of monoclinic phase often needs an incubation period of ~150 hour at 1300°C.[29] Therefore, it is reasonable to conclude that the multiconnection in the pore network is relatively unaffected by the phase change.
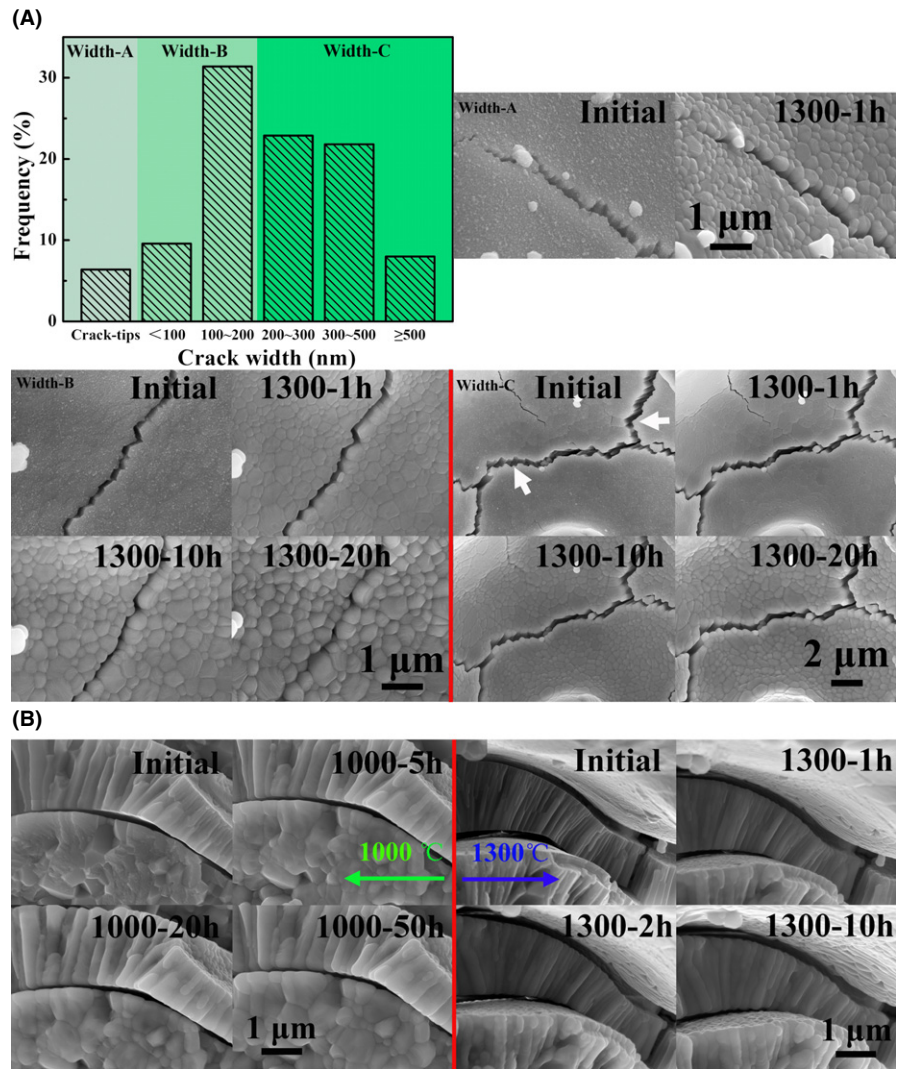
FIGURE 5 Quasi in situ healing observations of the intrasplat cracks and the intersplat pores at the stage-I: (A) width distribution of the intrasplat cracks and the healing of intrasplat cracks at corresponding widths thermally exposed at 1300°C (B) the healing of intersplat pores thermally exposed at 1000°C and 1300°C. [Color figure can be viewed at wileyonlinelibrary.com]

4 | MODEL DEVELOPMENT

4.1 | Statement of the problem

The experimental part on sintering behavior of PS-YSZ coatings can be concluded as follows: (i) the sintering process exhibits distinct two-stage kinetics; (ii) at the stage I with a higher sintering kinetics, multipoint connection of the counter-surfaces occurs at the intersplat pore tips, as well as a small quantity of intrasplat cracks; (iii) at the stage II, a slow healing occurs at both the residual wide intersplat pore parts and the wide intrasplat cracks. It is known that the intersplat pores often refer to the imperfect bonding between layers. Therefore, the healing of intersplat pores actually corresponds to the increase of intersplat bonding ratio, which would be the dominant structural change at the stage I.

4.2 | Evolution of the bonding ratio

At the as-deposited state, the intersplat pores are connected with the intrasplat cracks from layer to layer until the coating surface. Therefore, the mean bonding ratio of the as-deposited coatings was determined by the structural visualization reported previously.[33] However, the pore connectivity decreases significantly after thermal exposure. Based on this consideration, it is not appropriate to obtain the bonding ratio of the aged coatings by the infiltration-based structural visualization. Owing to the fact that the interlamellar bonding ratio is highly related to the intersplat pores, this study further determined the bonding ratio of the aged coatings through the residual length density of intersplat pores, as shown in the following formula:[32,33]

$$L_2 = \frac{HL_1}{\delta} \qquad (4)$$

$$\varepsilon = \frac{\xi HL_1}{L_2} = \xi\delta \qquad (5)$$

$$\alpha = (1 - \varepsilon) \times 100\% \qquad (6)$$

where H and L_1 refer to the coating thickness and length, respectively. L_2 is the whole length of interface between splats in the coating, δ is the mean splat thickness, ξ is the

residual 2D pore density, ε is the unbonded ratio contributed by 2D pores, and α is the bonding ratio.

The Equation (4) describes a same area between the stacked-layer structure and the structure with spreading layers. The Equation (5) describes a length ratio of the interlamellar pores (ξHL_1) with respect to the total interfacial length (L_2). Owing to the 2D characteristic of the interlamellar pores, this length ratio is actually the unbonded ratio contributed by the interlamellar pores. Correspondingly, the bonding ratio can be determined.

In order to get the evolution of bonding ratio from Equation (4) to (6), it is necessary to firstly get the mean thickness of splats and the as-deposited bonding ratio. The structural visualization exhibited that the as-deposited bonding ratio was approximately 28%, and that the mean splat thickness was approximately 1.5 μm. This is consistent with previous investigations.[32,46] Similar to the previous report,[18] the splat thickness can also be determined statistically from the cross-section of YSZ coatings and individual splats (see Figure 3B). The result was approximately 1-2.5 μm. Additionally, the bonding ratio of the as-deposited YSZ coatings is located in the range of 26%-31% according to Equation (4) to (6). Therefore, the as-deposited bonding ratio and the mean splat thickness can be taken as 28% and 1.5 μm, respectively.

Figure 6 shows bonding ratio evolution of the YSZ coatings as a function of thermal exposure duration time. Similar to the mechanical property, it is possible to observe that the increase of bonding ratio also appeared to exhibit a two-stage trend (see Figure 6B). A higher temperature often leads to a sharper increase, as well as a shorter stage-I. Correspondingly, the bonding ratio increased from 28% to approximately 50% at the stage-I.

4.3 | Model development

In this section, a structural model based on the PS-YSZ coating was developed (see Figure 7), in order to correlate the microstructural evolution with mechanical property. The essential feature of the PS-YSZ coatings is a lamellar structure with connected inter/intra-splat pore network.
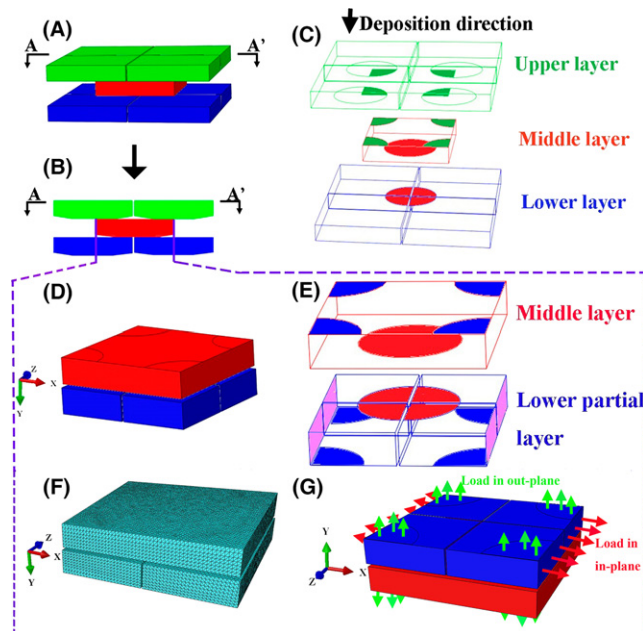

FIGURE 7 The developed structural model to predict the Young's modulus: (A) representative three bonded layers; (B) the cross-section along A-A′ in (A); (C) the separated three layers corresponding to (A), in order to present the bonding condition between neighboring layers; (D) a calculating unit adopted in ABAQUS; (E) the separated pattern of the calculating unit; (F) a meshed calculating unit in ABAQUS; (G) the displacement applied on a calculating unit to obtain Young's modulus. The green arrows along y-axis and the red arrows along x-axis aim to obtain the Young's modulus in the out-plane direction and in the in-plane direction, respectively [Color figure can be viewed at wileyonlinelibrary.com]

Consequently, the basic unit to compose a whole coating is the splat segments divided by intrasplat cracks.[18] Figures 7A-C describe the layer-stacking condition with representative three layers. For simplification, four structural units were presented in the upper layer and the lower layer, whereas only one structural unit was presented in the middle layer. The assumptions are as follows: (i) the splat segments are all assumed to be cubic shape with a same length and thickness, termed as a structural unit; (ii) the
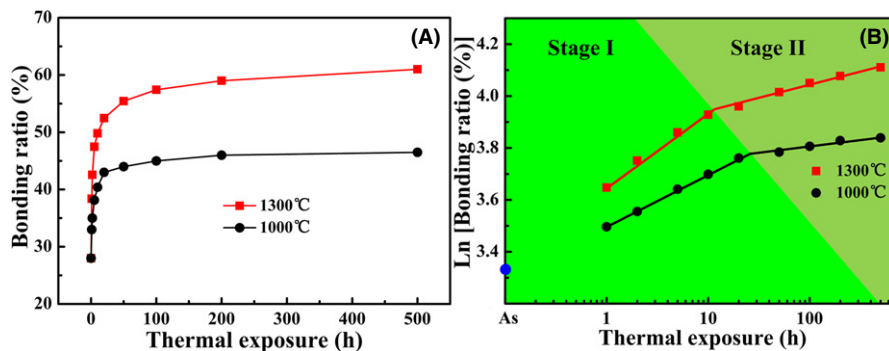

FIGURE 6 Evolution of bonding ratio determined using 2D pore length density: (A) the evolution of bonding ratio and (B) the bonding ratio evolution shown as Ln-t corresponding to (A). The As stands for the as-deposited state [Color figure can be viewed at wileyonlinelibrary.com]

circular bonded area is assumed to be located at the bottom center of a structural unit; (iii) the structural units are stacked on the lower layer uniformly. This means that every structural unit is exactly and equably located at the four corners of those four structural units in the lower layer; (iv) the intersplat pores separate the neighboring two layers partially, whereas the intrasplat cracks separate the structural unit completely in one layer; (v) at the stage I, the healing of intrasplat cracks is neglected. However, at the stage II, the healing of both the intersplat pores and the intrasplat cracks is considered.

The commercial FEM code ABAQUS was used to carry out the numerical calculation. Owing to the periodic symmetry of the developed model (see Figure 7A), a simplified periodic pattern is used for the numerical calculation, termed as a calculating unit (see the purple dotted box in Figure 7). Under this condition, a whole structure could be obtained by repeating the calculating unit along the three axes. Consequently, the macroscopic property could be determined using the calculating unit with appropriate periodic boundary conditions. In detail, the calculating unit was obtained by cutting the lower layer along the boundaries of the middle structural unit (see Figure 7D). The opposite cross-sections of the lower partial layer (see Figure 7E in pink color) will have consistent deformation behavior, since they would be bonded together when composing a whole structure. Similarly, the bonding areas in the middle layer and the lower partial layer (see Figure 7E in blue color) would also exhibit consistent deformation behavior. Based on this consideration, periodic boundary conditions were applied to these corresponding-pair surfaces, with the aim to realize the totally same strain behavior under stress. Other detailed procedure of the periodic boundary conditions can be found elsewhere.[47]

Herein, all structural units are taken to be homogeneous, isotropic, and linear elastic. Young's modulus and Poisson's ratio of the fully dense YSZ are taken as 205 GPa and 0.23,[48] respectively. The bonding between structural units is realized by the Tie constraints. The meshing procedure is carried out with 0.2 μm global seeds, accompanying with the Tet element shape, as shown in Figure 7F.

In this study, the x-z plane, which is perpendicular to the deposition direction, is taken as the reference plane. In the case of the in-plane Young's moduli, a uniform displacement is applied on the cross-sections (see Figure 7E in pink color) of the lower partial layer along x-axis, as shown in Figure 7G with red arrows. In the case of the out-plane Young's moduli, a uniform displacement is applied on the bonding areas (see Figure 7E in blue color) along y-axis, as shown in Figure 7G with green arrows. Subsequently, the stress-strain curve can be determined using the curve of reaction force-displacement. The other

details to obtain Young's moduli can be found in our previous report.[18]

4.4 | Results of model prediction

In the developed structural model, the Young's modulus often vary linearly with length and thickness.[18] Therefore, it is reasonable to select the mean value for numerical calculation. Similar to previous study,[18] this study determined the statistical segment length from coating surface, and the result was approximately 6-15 μm. Consequently, the mean length and the thickness of a structural unit are selected to be 10 and 1.5 μm, respectively.

Figure 8 shows the evolution of Young's modulus as a function of bonding ratio. It can be observed from Figure 8B that the increase trends of Young's modulus were consistent with each other using three values of thickness. This confirmed the rationality to select the mean value for numerical calculation. Regarding the effect of bonding ratio on the Young's modulus, the results are at least twofold. On the one hand, it is possible to observe that the increase of bonding ratio has a significant effect on the Young's modulus in both directions. This is consistent with the previous report.[21] On the other hand, the increase of Young's modulus as a function of bonding ratio is nonlinear, i.e., the initial increase of bonding ratio has a more distinct effect on the increase of Young's modulus (see Figure 8B). Commonly, the mean bonding ratio of the APS ceramic coatings is approximately 10%-32%.[33,46,49] In this study, the measured bonding ratio is approximately 28%. During the stage-I, the bonding ratio increased from 28% to 50% (see Figure 6). Corresponding to this bonding ratio range (28%-50%), the increment of the Young's modulus in the out-plane direction is much higher than that in the in-plane direction (see Figure 8C). The predicted anisotropic increasing trend of Young's modulus is consistent with the experimental results (see Figure 2B), in which the microscopic Young's modulus in the out-plane direction increases more rapidly than that in the in-plane direction. This may confirmed qualitatively that the healing of intersplat pores plays a dominant role on the structural change at the stage-I, since only the interlamellar healing was considered at this stage.

5 | DISCUSSION: COMPARISON BETWEEN MODEL PREDICTION AND EXPERIMENTAL RESULTS

The PS-YSZ coatings exhibit a complicated structure with connected pore network, suggesting that their sintering behavior is both material and structure specific. A sintering model developed by Cipitria et al.[7,27] captured this issue,
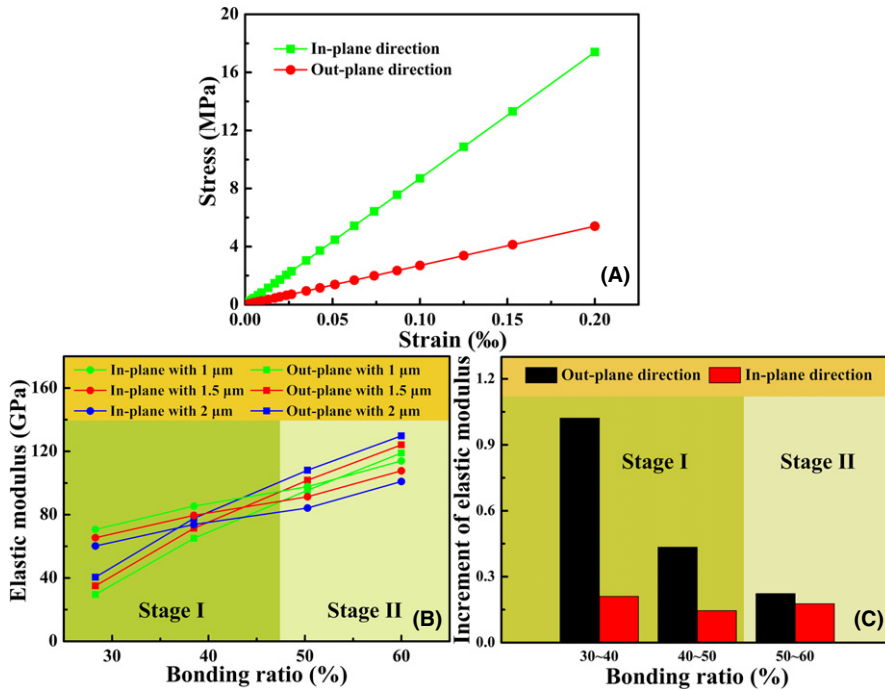
FIGURE 8 Evolution of the Young's modulus as a function of bonding ratio: (A) the stress-strain curves obtained from a curve of reaction force-displacement under a bonding ratio of 28%; (B) the evolution of Young's modulus as a function of bonding ratio with different splat thicknesses; and (C) the increment of Young's modulus in different ranges of bonding ratio under the splat thickness of 1.5 μm [Color figure can be viewed at wileyonlinelibrary.com]

and gave a consistent prediction on the overall sintering process. In detail, their comparisons[7] between model prediction and experimental results are shown in Figure 9, which is presented as Ln-t curves. It is obvious that their model failed to exhibit the aging stage-sensitive sintering kinetics.

In the case of the thermal conductivity (see Figure 9A), a distinct two-stage trend can be observed for the experimental results. However, the model prediction exhibited a linear increase trend until saturation. Therefore, the mechanical and thermal properties determined by experiments both exhibited a two-stage evolutionary trend, which cannot be captured by the typical sintering model.[7] It is known that the degradation of thermal insulation is a comprehensive healing result of the connected pore network.[17] However, the linear contraction in a given direction is primarily attributed to the healing of the corresponding vertical cracks, as shown in Figure 9B.

In the case of the through-thickness linear contraction, which depends on the healing of intersplat pores, the experimental results also exhibited an obvious two-stage evolutionary trend. However, the model prediction appeared to be almost linear increase. The increase rate was similar to the second increase stage of the experimental results. In the case of the in-plane linear contraction dependent with the healing of intrasplat cracks, the experimental results and the model prediction exhibited a similar linear increase. The initial fast increase stage was not so distinct as the linear contraction in through-thickness direction.

The reasons for these discrepancies could go back to the assumptions made on the sintering model.[7] The main assumption is that the 2D pores were all assumed to be equally thick. Consequently, the crack healing would proceed from two tips to center without multipoint connection. This is reasonable for most of the intrasplat cracks based on the experimental observation (see Figure 3A). Therefore, the linear contraction of model prediction in the in-plane direction is well consistent with the experimental results. However, multiconnection-induced rapidly healing occurs at almost every intersplat pore tip at the stage-I.
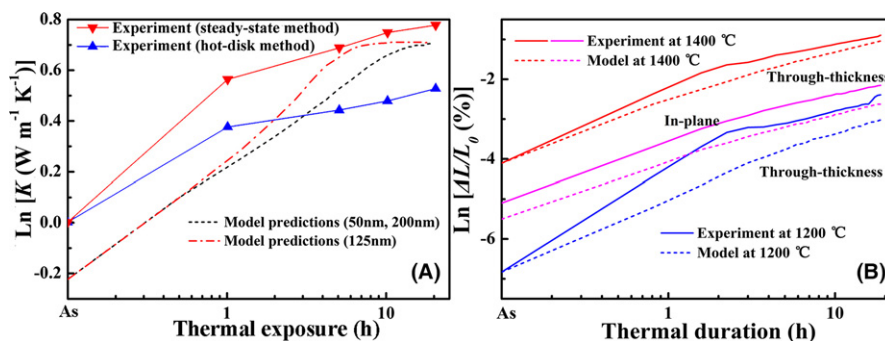

FIGURE 9 Comparisons between model prediction[7] and experimental data[7] presented as Ln-t curves: (A) thermal conductivity in through-thickness direction and (B) linear contractions. The As stands for the as-deposited state [Color figure can be viewed at wileyonlinelibrary.com]

Consequently, a two-stage evolutionary trend of the linear contraction could be observed in the through-thickness direction. On the one hand, it confirms that the ultrafast sintering kinetics at the stage-I is primarily attributed to the healing of intersplat pore tips. On the other hand, it can be concluded that the sintering procedure without multiconnection, as described in the typical sintering model,[7] cannot be applied to the healing of intersplat pores at the stage-I.

In this study, a faster sintering kinetic at the stage I results in a faster increase on the bonding ratio. By developing a structural model to simulate the evolution of pore healing at different stages, a more reasonable relationship between mechanical property and microstructural evolution could be obtained during overall thermal exposure duration. The indentation impression of Knoop indentation is approximately 70-100 μm, whereas the length of a splat segment is approximately 10-20 μm.[18] Therefore, the measured region of Knoop indentation is just several splat segments. In other words, the Knoop indentation is more informative to reflect the very essential microstructural characteristics of the PS-YSZ coatings.[18] Figure 10 shows the comparisons between model prediction and the microscopic Young's modulus in this study. It can be observed that the model prediction exhibited a two-stage evolutionary trend, which is consistent with the experimental data. In detail, the ultrafast increase rate of Young's modulus at the stage-I was captured preferably based on the fast increase of bonding ratio. This suggested that the increase of bonding ratio is primarily responsible for the structural change at the stage-I. At the stage-II, the evolution of Young's modulus was attributed to the healing of connected pore network with a relatively slower kinetics.

To sum up, the structural model predicted a two-stage evolutionary trend of the mechanical property, which is well consistent with the experimental results. To begin with, the intrinsic characteristics of the PS-YSZ coatings at the as-deposited state were captured properly, which provided a good foundation for the further microstructural evolution. Secondly, the revealing of the dominant microstructural changes at different stages guaranteed the sintering process based on the as-deposited state. At the stage-I, the large quantity of intersplat pore tips provided a higher possibility to realize a rapid healing induced by the multipoint connection. At the following stage-II, the residual wide intersplat pore parts, as well as the intrasplat cracks decreased the possibility of multiconnection between counter-surfaces. Consequently, the further healing would proceed primarily from two tips to center without multiconnection, as described in the typical sintering model.[7] Therefore, a slower sintering kinetics was presented at the stage-II. It is reported that the sizes and separations of intersplat pores are highly dependent with the morphologies of starting powders and process conditions.[15,16,20] The sintering would be thereby affected significantly. By revealing the sintering mechanism of TBCs related to the pore network, it is possible to realize structural tailoring by optimizing the process conditions, as well as the powder selection. In a companion paper (Part II), the detailed reasons responsible for the ultrafast sintering kinetics at the stage I would be discussed.

6 | CONCLUSIONS

In this study, a comprehensive understanding on the sintering behavior of PS-YSZ coatings was obtained. The
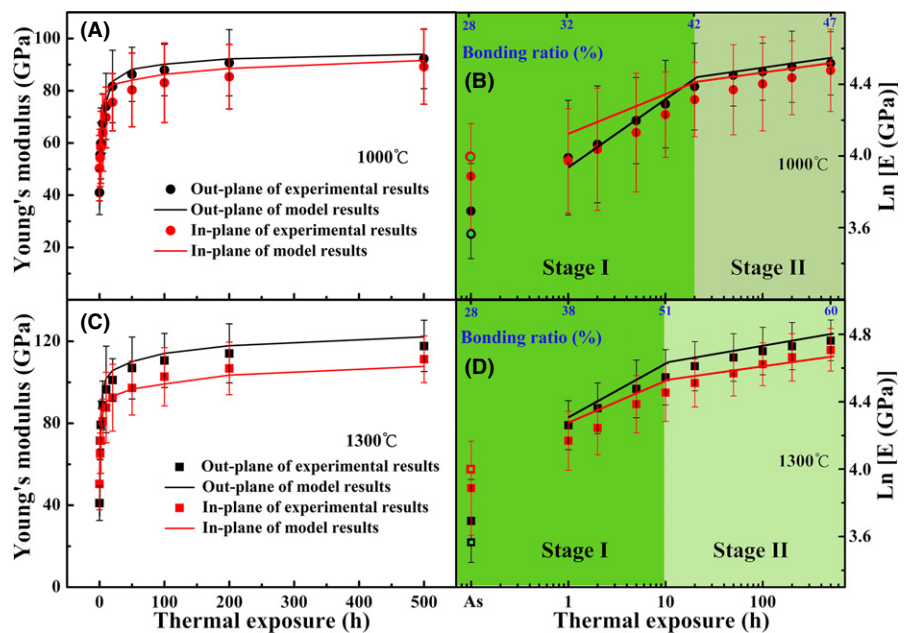

FIGURE 10 Comparison between model prediction and experimental results in this study: (A, B) 1000°C and (C, D) 1300°C. (B) and (D) are the Ln-t curves corresponding to (A) and (C), respectively. The dark and light green refer to fast and slow increase kinetics, respectively. The As stands for the as-deposited state [Color figure can be viewed at wileyonlinelibrary.com]

healing of 2D pores was aging stage-sensitive, resulting in a two-stage evolutionary trend of mechanical property. The detailed conclusions are as follows:

1. At the as-deposited state, the intersplat pores appeared to be wedge-like, whereas the intrasplat cracks exhibit an equal-thick morphology.
2. At the stage-I, a rapid healing induced by multipoint connection occurred at the intersplat pore tips, as well as a small quantity of narrow intrasplat cracks, which is responsible for the ultrafast sintering kinetics at this stage.
3. At the following stage-II, the residual wide intersplat pore parts and the wide intrasplat cracks decreased the possibility of multipoint connection at their counter-surfaces. Consequently, the further healing would proceed primarily from two tips to center without multiconnection, resulting in a much lower sintering kinetic at this stage.
4. A structural model was developed based on the microstructure of PS-YSZ coatings, in order to comprehensively understand the quantitative evolution of coating properties. The model predicted a two-stage evolutionary trend, which is consistent with the experimental data. This confirmed the healing behavior of the intersplat pores and the intrasplat cracks at different thermal exposure stages.

Finally, a comprehensive understanding on the sintering behavior of PS-YSZ coatings can contribute greatly to prolonging the service life span of TBCs, by reasonably tailoring the microstructure and the pore distribution in the top-coat of TBCs.

ACKNOWLEDGMENTS

REFERENCES

1. Padture NP, Gell M, Jordan EH. Materials science - thermal barrier coatings for gas-turbine engine applications. *Science*. 2002;296:280-284.
2. Sampath S, Schulz U, Jarligo MO, Kuroda S. Processing science of advanced thermal-barrier systems. *MRS Bull*. 2012;37:903-910.
3. Chi WG, Sampath S, Wang H. Microstructure-thermal conductivity relationships for plasma-sprayed yttria-stabilized zirconia coatings. *J Am Ceram Soc*. 2008;91:2636-2645.
4. Kulkarni AA, Goland A, Herman H, et al. Microstructure-property correlations in industrial thermal barrier coatings. *J Am Ceram Soc*. 2004;87:1294-1300.
5. Dwivedi G, Viswanathan V, Sampath S, Shyam A, Lara-Curzio E. Fracture toughness of plasma-sprayed thermal barrier ceramics: influence of processing, microstructure, and thermal aging. *J Am Ceram Soc*. 2014;97:2736-2744.
6. Hasselman DPH, Johnson LF, Bentsen LD, Syed R, Lee HL, Swain MV. Thermal-diffusivity and conductivity of dense polycrystalline ZrO_2 ceramics - a survey. *Am Ceram Soc Bull*. 1987;66:799-806.
7. Cipitria A, Golosnoy IO, Clyne TW. A sintering model for plasma-sprayed zirconia TBCs. Part I: free-standing coatings. *Acta Mater*. 2009;57:980-992.
8. Chen DY, Gell M, Jordan EH, Cao E, Ma XQ. Thermal stability of air plasma spray and solution precursor plasma spray thermal barrier coatings. *J Am Ceram Soc*. 2007;90:3160-3166.
9. Thompson JA, Clyne TW. The effect of heat treatment on the stiffness of zirconia top coats in plasma-sprayed TBCs. *Acta Mater*. 2001;49:1565-1575.
10. Fauchais P, Fukumoto M, Vardelle A, Vardelle M. Knowledge concerning splat formation: an invited review. *J Therm Spray Technol*. 2004;13:337-360.
11. Paul S, Cipitria A, Tsipas SA, Clyne TW. Sintering characteristics of plasma sprayed zirconia coatings containing different stabilisers. *Surf Coat Tech*. 2009;203:1069-1074.
12. Clyne TW, Gill SC. Residual stresses in thermal spray coatings and their effect on interfacial adhesion: a review of recent work. *J Therm Spray Techn*. 1996;5:401-418.
13. Liu Y, Nakamura T, Srinivasan V, Vaidya A, Gouldstone A, Sampath S. Non-linear elastic properties of plasma-sprayed zirconia coatings and associated relationships with processing conditions. *Acta Mater*. 2007;55:4667-4678.
14. Tan Y, Longtin JP, Sampath S, Wang H. Effect of the starting microstructure on the thermal properties of as-sprayed and thermally exposed plasma-sprayed YSZ coatings. *J Am Ceram Soc*. 2009;92:710-716.
15. Deshpande S, Kulkarni A, Sampath S, Herman H. Application of image analysis for characterization of porosity in thermal spray coatings and correlation with small angle neutron scattering. *Surf Coat Tech*. 2004;187:6-16.
16. Wang Z, Kulkarni A, Deshpande S, Nakamura T, Herman H. Effects of pores and interfaces on effective properties of plasma sprayed zirconia coatings. *Acta Mater*. 2003;51:5319-5334.
17. Xie H, Xie YC, Yang GJ, Li CX, Li CJ. Modeling thermal conductivity of thermally sprayed coatings with intrasplat cracks. *J Therm Spray Techn*. 2013;22:1328-1336.
18. Li GR, Lv BW, Yang GJ, Zhang WX, Li CX, Li CJ. Relationship between lamellar structure and elastic modulus of thermally sprayed thermal barrier coatings with intra-splat cracks. *J Therm Spray Techn*. 2015;24:1355-1367.
19. Kulkarni A, Wang Z, Nakamura T, et al. Comprehensive microstructural characterization and predictive property modeling of plasma-sprayed zirconia coatings. *Acta Mater*. 2003;51:2457-2475.
20. Tan Y, Longtin JP, Sampath S. Modeling thermal conductivity of thermal spray coatings: comparing predictions to experiments. *J Therm Spray Techn*. 2006;15:545-552.
21. Tan Y, Shyam A, Choi WB, Lara-Curzio E, Sampath S. Anisotropic elastic properties of thermal spray coatings determined via resonant ultrasound spectroscopy. *Acta Mater*. 2010;58:5305-5315.

22. Leigh SH, Lin CK, Berndt CC. Elastic response of thermal spray deposits under indentation tests. *J Am Ceram Soc*. 1997;80:2093-2099.

23. Cernuschi F, Bison PG, Marinetti S, Scardi P. Thermophysical, mechanical and microstructural characterization of aged free-standing plasma-sprayed zirconia coatings. *Acta Mater*. 2008;56:4477-4488.

24. Vassen R, Czech N, Mallener W, Stamm W, Stover D. Influence of impurity content and porosity of plasma-sprayed yttria-stabilized zirconia layers on the sintering behaviour. *Surf Coat Tech*. 2001;141:135-140.

25. Ratzer-Scheibe HJ, Schulz U. The effects of heat treatment and gas atmosphere on the thermal conductivity of APS and EB-PVD PYSZ thermal barrier coatings. *Surf Coat Tech*. 2007;201:7880-7888.

26. Anderson PS, Wang X, Xiao P. Effect of isothermal heat treatment on plasma-sprayed yttria-stabilized zirconia studied by impedance spectroscopy. *J Am Ceram Soc*. 2005;88:324-330.

27. Cipitria A, Golosnoy IO, Clyne TW. A sintering model for plasma-sprayed zirconia thermal barrier coatings. Part II: coatings bonded to a rigid substrate. *Acta Mater*. 2009;57:993-1003.

28. Tan Y, Longtin JP, Sampath S, Zhu DM. Temperature-gradient effects in thermal barrier coatings: an investigation through modeling, high heat flux test, and embedded sensor. *J Am Ceram Soc*. 2010;93:3418-3426.

29. Yang GJ, Chen ZL, Li CX, Li CJ. Microstructural and mechanical property evolutions of plasma-sprayed YSZ coating during high-temperature exposure: comparison study between 8YSZ and 20YSZ. *J Therm Spray Techn*. 2013;22:1294-1302.

30. Ilavsky J, Stalick JK. Phase composition and its changes during annealing of plasma-sprayed YSZ. *Surf Coat Tech*. 2000;127:120-129.

31. Trice RW, Su YJ, Mawdsley JR, et al. Effect of heat treatment on phase stability, microstructure, and thermal conductivity of plasma-sprayed YSZ. *J Mater Sci*. 2002;37:2359-2365.

32. Liu T, Luo XT, Chen X, Yang GJ, Li CX, Li CJ. Morphology and size evolution of interlamellar two-dimensional pores in plasma-sprayed $La_2Zr_2O_7$ coatings during thermal exposure at 1300°C. *J Therm Spray Techn*. 2015;24:739-748.

33. Li CJ, Wang WZ. Quantitative characterization of lamellar microstructure of plasma-sprayed ceramic coatings through visualization of void distribution. *Mat Sci Eng A-Struct*. 2004;386:10-19.

34. Zhou T, Nie PL, Lv HP, Chen QL, Cai X. Assessment of elastic properties of coatings by three-point bending and nanoindentation. *J Coat Technol Res*. 2011;8:355-361.

35. Lima RS, Kruger SE, Lamouche G, Marple BR. Elastic modulus measurements via laser-ultrasonic and knoop indentation techniques in thermally sprayed coatings. *J Therm Spray Techn*. 2005;14:52-60.

36. Guo S, Kagawa Y. Young's moduli of zirconia top-coat and thermally grown oxide in a plasma-sprayed thermal barrier coating system. *Scripta Mater*. 2004;50:1401-1406.

37. Tsipas SA, Golosnoy IO, Damani R, Clyne TW. The effect of a high thermal gradient on sintering and stiffening in the top coat of a thermal barrier coating system. *J Therm Spray Techn*. 2004;13:370-376.

38. Sevostianov I, Kachanov M. Modeling of the anisotropic elastic properties of plasma-sprayed coatings in relation to their microstructure. *Acta Mater*. 2000;48:1361-1370.

39. Kroupa F, Dubsky J. Pressure dependence of young's moduli of thermal sprayed materials. *Scripta Mater*. 1999;40:1249-1254.

40. Allen AJ, Long GG, Boukari H, et al. Microstructural characterization studies to relate the properties of thermal-spray coatings to feedstock and spray conditions. *Surf Coat Tech*. 2001;146:544-552.

41. Allen AJ, Ilavsky J, Long GG, Wallace JS, Berndt CC, Herman H. Microstructural characterization of yttria-stabilized zirconia plasma-sprayed deposits using multiple small-angle neutron scattering. *Acta Mater*. 2001;49:1661-1675.

42. Markocsan N, Nylen P, Wigren J, Li XH, Tricoire A. Effect of thermal aging on microstructure and functional properties of zirconia-base thermal barrier coatings. *J Therm Spray Techn*. 2009;18:201-208.

43. Olevsky EA. Theory of sintering: from discrete to continuum. *Mater Sci Eng, R*. 1998;23:41-100.

44. Ilavsky J, Long GG, Allen AJ, Berndt CC. Evolution of the void structure in plasma-sprayed YSZ deposits during heating. *Mater Sci Eng A-Struct*. 1999;272:215-221.

45. Erk KA, Deschaseaux C, Trice RW. Grain-boundary grooving of plasma-sprayed yttria-stabilized zirconia thermal barrier coatings. *J Am Ceram Soc*. 2006;89:1673-1678.

46. Li CJ, Ohmori A. Relationships between the microstructure and properties of thermally sprayed deposits. *J Therm Spray Techn*. 2002;11:365-374.

47. Zhang WX, Wang TJ, Li LX. Numerical analysis of the transverse strengthening behavior of fiber-reinforced metal matrix composites. *Comp Mater Sci*. 2007;39:684-696.

48. Lu XJ, Xiao P. Constrained sintering of YSZ/Al_2O_3 composite coatings on metal substrates produced from eletrophoretic deposition. *J Eur Ceram Soc*. 2007;27:2613-2621.

49. Ohmori A, Li CJ. Quantitative characterization of the structure of plasma-sprayed Al_2O_3 coating by using copper electroplating. *Thin Solid Films*. 1991;201:241-252.